Materials Today Chemistry 47 (2025) 102860

Contents lists available at ScienceDirect

Materials Today Chemistry

journal homepage: www.journals.elsevier.com/materials-today-chemistry/

Synthesis and electrochemical behaviour of titanium niobates: A step toward stable anode materials

A. Calvo-Villoslada [a,*], M.L. López [b], P. Almodóvar [c], P. Fernández [a], I. Álvarez-Serrano [b], B. Sotillo [a,**]

[a] Department of Material Physics, Faculty of Physics, Complutense University of Madrid, 28040, Madrid, Spain
[b] Department of Inorganic Chemistry, Faculty of Chemistry, Complutense University of Madrid, 28040, Madrid, Spain
[c] Zelestium Technologies S.L, Spain

ARTICLE INFO

Keywords:
Niobates
Titanium
Niobium
Mixed oxides
Lithium-ion batteries
Hydrothermal synthesis
Anodes

ABSTRACT

Previous studies have demonstrated the potential long-term cyclability and stability of TNOs as electrodes in LIBs. However, the wide variety of stoichiometries of TNOs has complicated the study of the physicochemical properties of this material, which can change greatly between different phases, compositions and structures. In this study, two TNO compositions ($TiNb_2O_7$ and $Ti_2Nb_{10}O_{29}$) have been synthesized via solid-state and hydrothermal synthesis. A detailed electrochemical characterization as electrodes for LIBs has been performed. A capacity of 257.3 mA h g^{-1} has been obtained with losses <6 % after 300 cycles at 1C for the hydrothermal route of the $Ti_2Nb_{10}O_{29}$ composition. Additionally, a complete recovery of capacity was observed after cycling at higher velocities (5C, 10C).

1. Introduction

The development of energy storage devices is one of the most researched areas in the industry. Among various battery technologies, lithium-ion batteries (LIBs) are the most widely used due to their high capacity and efficient charge/discharge performance at multiple rates [1]. The most common anode material for LIBs is graphite, primarily due to its low manufacturing cost and ease of scalability while maintaining good capacity values [2–5]. However, graphite anodes suffer from structural degradation through operation, leading to poor long-term cycling performance. This issue presents a significant challenge, especially as the demand for LIBs with improved performances increases alongside technological advancements, such as the electrification of the automotive sector [6]. To meet these growing demands, more stable and higher-performance electrode materials are essential.

Titanium Niobates (TNOs) are among the most promising alternatives for LIB anodes, offering higher capacity and stability than the most used industry electrodes. TNOs are more stable and reliable than both graphite and $Li_4Ti_5O_{12}$, while also exhibiting higher capacity values (388–402 mA h g^{-1}, depending on the stoichiometry) compared to graphite (372 mA h g^{-1}), $Li_4Ti_5O_{12}$ (175 mA h g^{-1}), and other less common alternatives like TiO_2 (335 mA h g^{-1}) [5].

TNOs (with general formula $TiNb_xO_y$) can exhibit two main crystal structures with different symmetries, depending on the synthesis conditions and stoichiometry: orthorhombic and monoclinic. Monoclinic structure is the one shared for most of the titanium niobates compounds [5]. It follows the Wadsley-Roth crystal structure, first described by Wadsley and Roth in niobium-based systems [7]. In these structures, transition metal atoms (in our case, Nb or Ti) are positioned at the centre of octahedra, which are coordinated with six oxygen atoms at each vertex. These octahedra connect to form a lattice similar to ReO_3, where each octahedron shares its vertices with adjacent octahedra. However, the key difference between the ReO_3 lattice and the Wadsley-Roth structure arises from the redox properties of the niobium-based systems. In Wadsley-Roth structure, oxygen deficiencies are accommodated by changing from corner-shared octahedra to edge-shared octahedra, forming crystallographic shear planes [7,8]. Some studies [9,10] suggested that this kind of edge-shared octahedra is where the titanium in TNO will be preferably located, due to the charge of the cations. $TiNb_2O_7$ and $Ti_2Nb_{10}O_{29}$ are the most extensively studied stoichiometries for LIBs due to their high stability. Crystal structures for $TiNb_2O_7$ (3 × 3 ReO_3-type blocks) and $Ti_2Nb_{10}O_{29}$ (4 × 3 ReO_3-type blocks) are

* Corresponding author.
** Corresponding author.
E-mail addresses: aaroncal@ucm.es (A. Calvo-Villoslada), bsotillo@ucm.es (B. Sotillo).

https://doi.org/10.1016/j.mtchem.2025.102860
Received 26 March 2025; Received in revised form 23 June 2025; Accepted 28 June 2025
Available online 2 July 2025

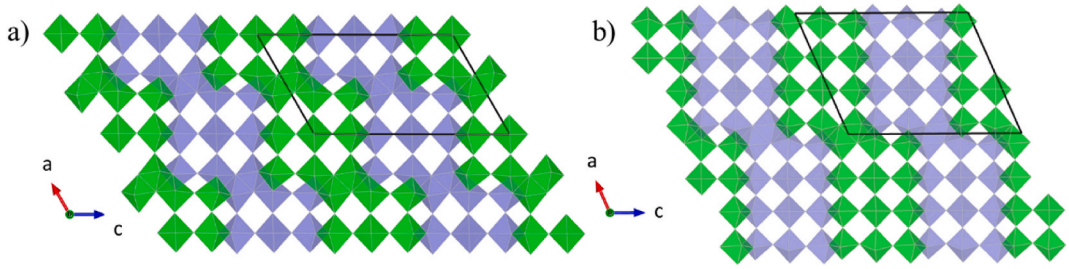

Fig. 1. Crystal structure of monoclinic phases for (a) $TiNb_2O_7$ (3 × 3 ReO_3-type blocks) and (b) $Ti_2Nb_{10}O_{29}$ (4 × 3 ReO_3-type blocks). Blue and green octahedra represents ReO_3-type blocks located at different planes perpendicular to b-axis. The structures have been plotted using VESTA software [13].

Table 1
Notation and characteristics of each studied sample.

Sample Name	Stoichiometry	Ratio Nb:Ti	Synthesis Method
TNO12Ox	$TiNb_2O_7$	2:1	Solid-State from Oxides
TNO12HT	$TiNb_2O_7$	2:1	Hydrothermal
TNO15Ox	$Ti_2Nb_{10}O_{29}$	5:1	Solid-State from Oxides
TNO15HT	$Ti_2Nb_{10}O_{29}$	5:1	Hydrothermal

shown in Fig. 1, which are the most representative phases of TNOs [11,12].

The Wadsley-Roth structure produces a 3D open crystalline network, which is known for its stability and resistance in oxidation reduction applications, particularly in lithium-ion batteries [8,14,15]. Due to its open lattice, lithium-ion insertion induces less structural stress compared to more compact configurations. Also, the covalent character of the bonds makes the TNO more stable than the graphite electrodes usually used [3,16].

Although both compositions studied differ little in their electrochemical capacity, with $TiNb_2O_7$ having a theorical capacity of 388 mA h g^{-1}, and $Ti_2Nb_{10}O_{29}$ reaching 396 mA h g^{-1} [5,8] by modifying the synthesis route, various morphologies and micro/nanostructures can be obtained, significantly influencing the electrochemical performance of TNOs [3].

In this work, we present a comparative study of two monoclinic TNO phases ($TiNb_2O_7$ and $Ti_2Nb_{10}O_{29}$) synthesized via both solid-state and hydrothermal methods, with a focus on exploring the synergistic effects of composition, synthesis route, and microstructure on electrochemical behaviour. We employ niobium oxalate hydrate in hydrothermal synthesis, offering a cleaner and more controlled alternative to the commonly used niobium chloride [17] or ammonium niobium oxalate [18], which introduces additional ionic species that may complicate phase purity and reproducibility, and produces corrosive compounds (HCl, NH_3). Additionally, the electrodes were prepared using sodium alginate as the binder, a sustainable and water-processable agglomerant that contributes to improved mechanical integrity and environmental compatibility. Our study bridges the gap between morphology engineering and phase stability in TNOs, demonstrating a remarkable combination of long-term cycling stability, fast rate performance, and thermal resilience. The integrated structural–electrochemical insights provided here contribute meaningfully to the rational design of high-performance anode materials.

2. Materials and methods

2.1. Synthesis

The synthesis routes selected in this work are solid-state reaction (also known as ceramic method) and hydrothermal synthesis. Whereas the solid-state reaction is commonly employed, hydrothermal route is less used for the synthesis of TNOs [3]. On the other hand, the use of niobium oxalate as precursor has been rarely reported. The samples characteristics and their associated notation are shown in Table 1.

For the solid-state synthesis, Nb_2O_5 (99.9985 % purity, Alfa Aesar) and TiO_2 (Anatase, 99.99 % purity, Sigma-Aldrich) powders were pressed (1 t) into round pellets of 7 mm diameter. These pellets were ground using an agate mortar and pressed again into pellets with the same specifications to ensure a better oxide mixture. Subsequently, the pellets were heated in a furnace at 1300 °C for 24 h.

For the hydrothermal synthesis, the precursors used were titanium acetylacetonate $C_{10}H_{14}O_5Ti$ (97 % purity, Merck) and niobium oxalate hydrate (V) $Nb(HC_2O_4)_5 \cdot x\ H_2O$ (Alfa Aesar). Both were dissolved in distilled water and mixed in an autoclave with a small quantity of ammonia NH_3 (1.5 mlL). After this, the autoclave was heated for 24 h at 220 °C. The white powder obtained was filtered and calcined first for 4 h at 600 °C, followed by 4 h at 800 °C. Hydrothermal synthesis has been previously essayed mainly from niobium chloride [3], which hydrolysis leads to hydrochloric acid. We selected niobium oxalate as an alternative precursor, with no other elements apart from Nb, C, O and H, ensuring precise stoichiometric control and better reproducibility in high-performance formulations.

2.2. Experimental techniques

Scanning Electron Microscopy (SEM) imaging was performed using a FEI Inspect-S SEM at 20 kV. X-ray Energy Dispersive Spectroscopy (XEDS) characterization was made with a Bruker QUANTAX 70 detector connected to a Hitachi TM3000 SEM working at 15 kV. X-ray Diffraction (XRD) measurements were carried out using a PANalytical X'Pert Powder diffractometer in Bragg-Brentano geometry with Cu-Kα radiation, using a step of 0.05° in 2θ and 1 s counting time. Micro-Raman (μ-Raman) spectra were recorded with a Horiba JobinYvon LABRAM-HR confocal microscope, by exciting the sample with a 632.8 nm He–Ne laser, focused through a 10 × Olympus objective (0.25 NA). To analyse the collected signal, a 600 l/mm diffraction grating was employed, and the data was obtained with a Synapse 354308 CCD camera. High-Resolution Transmission Electron Microscopy (HRTEM) was done using a JEM 3000F.

The half-cell batteries were assembled in Swagelok cells. The electrodes were prepared by mixing 70 % active material (TNO), 20 % Carbon C65 (Imerys), and 10 % sodium alginate (Sigma-Aldrich) in distilled water until a paint-like consistency was achieved. The resulting mixture was spread onto a copper sheet to form the electrode. A borosilicate (Whatman GF/D) membrane was used as the separator, and the electrolyte consisted of 1 M $LiPF_6$ in EC:DMC (1:1 by weight). The reference electrode (anode) was a metallic lithium sheet, and the assembly was carried out in an argon-filled glovebox.

Electrochemical characterization of the half-cell batteries was performed using a Biologic 815 system. Cyclic voltammetry (CV) was conducted over potential ranges of 0.01–3 V and 1–3 V. Galvanostatic Cycling with Potential Limitation (GCPL) was done at various charge/discharge rates. The cycling rate is denoted as 'C', where 1C corresponds to the current required to fully charge the theoretical electrode capacity in 1 h and discharge it in another hour. A rate of 2C is twice as fast as 1C,

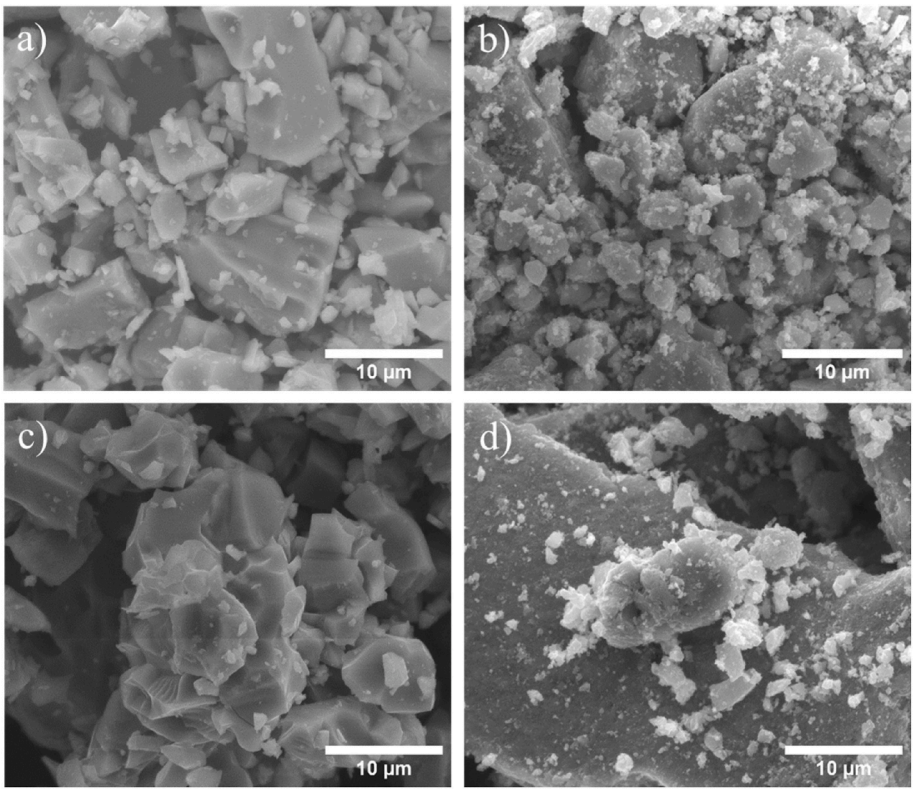

Fig. 2. SEM images of a) TNO12Ox, b) TNO12HT, c) TNO15Ox, d) TNO15HT.

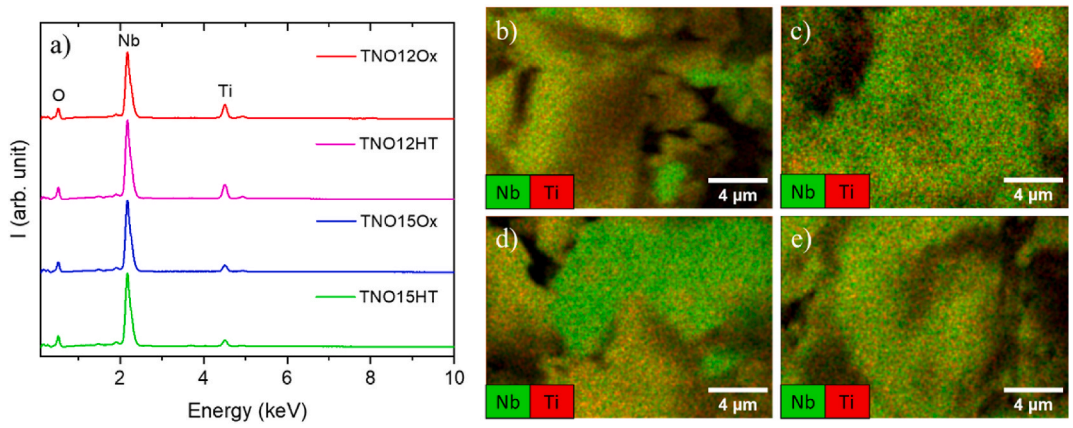

Fig. 3. a) XEDS spectra of all the studied samples. b) XEDS mapping of TNO12Ox, c) TNO12HT, d) TNO15Ox, e) TNO15HT.

while C/5 is five times slower. Additionally, Potentiostatic Electrochemical Impedance Spectroscopy (PEIS) analysis was conducted, by applying an AC voltage of 5 mV over a frequency range of 0.01–100 kHz.

Table 2
Atomic Nb/Ti ratios obtained by XEDS of all the samples, showing the mean ratio and the values for the particles with the maximum and minimum Nb/Ti ratios observed.

Nb/Ti Ratio	Mean value	Maximum Nb/Ti	Minimum Nb/Ti
TNO12Ox	2.1	2.9	1.6
TNO12HT	2.1	2.2	1.3
TNO15Ox	4.7	10.1	2.2
TNO15HT	4.9	5.7	2.7

3. Results and discussion

3.1. Structural and compositional characterization

The morphology of the obtained samples varies significantly depending on the synthesis route used. Both compositions ($TiNb_2O_7$ and $Ti_2Nb_{10}O_{29}$) show similar structures when synthesized using the same technique. As shown in the SEM images in Fig. 2 (a) and (c), samples obtained via solid-state synthesis form microcrystals of various sizes, ranging from less than 10 μm in length and width to larger particles measuring tens of micrometres. In contrast, samples obtained using hydrothermal synthesis (Fig. 2 (b) and (d)) appear as agglomerates of nanoparticles. These agglomerates also display a wide size distribution, with sizes ranging from 1 to tens of microns. These differences agree with the observations reported by other authors [3], as hydrothermal routes favour the obtention of nanoparticles.

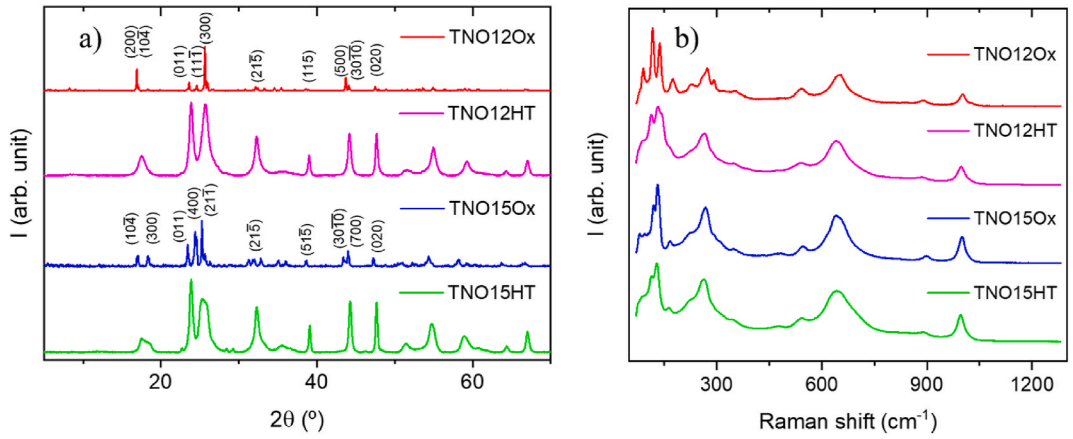

Fig. 4. a) XRD measurements and b) μ-Raman spectra of each sample.

To analyse the composition of the obtained samples, multiple techniques have been employed. As shown in Fig. 3(a), XEDS spectra clearly confirm the absence of any unwanted element, with the main peaks corresponding to the characteristic X-ray lines of niobium, titanium, and oxygen. The XEDS mappings in Fig. 3(b)–(e) reveal a significant difference in the homogeneity of niobium and titanium distributions depending on the synthesis route used. Samples obtained via solid-state reaction exhibit a less homogeneous distribution compared to their hydrothermal counterparts. This difference is further illustrated in Table 2, where the quantified niobium-to-titanium ratios show greater variation between extreme values and the mean in solid-state synthesis samples, whereas hydrothermal synthesis yields a more consistent distribution. This observation is coherent considering that solid-state reaction relies on diffusion to obtain the desired composition. Despite these variations, Table 2 also confirms that the mean niobium-to-titanium ratio for each composition aligns well with the expected stoichiometries. Additionally, extreme ratios found in some grains can be associated to other known TNO compositions (like $Ti_5Nb_{44}O_{120}$, $Ti_3Nb_{34}O_{91}$ or $Ti_2Nb_2O_{19}$) [11,12].

To ensure the successful synthesis of TNOs and discard the presence of a binary oxide mixture (TiO_2 and Nb_2O_5), XRD as well as μ-Raman spectroscopy have been used. Fig. 4 presents a comparative overview of

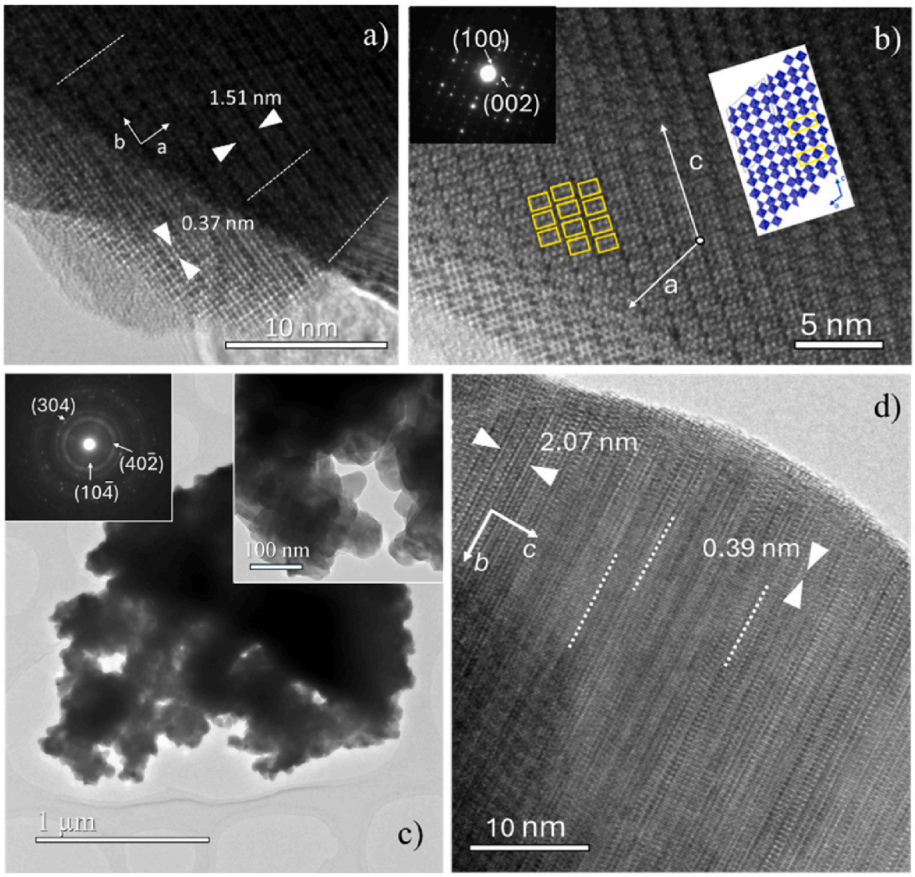

Fig. 5. HRTEM images for TNO15-ox a) *a* - *b* plane and b) *a* - *c* plane. Insets in b) gather corresponding ED pattern and a structural scheme showing the observed blocks in yellow squares; HRTEM images for TNO15-ox; c) low-magnification image with (in insets) corresponding ED pattern and a detailed image for TNO15-HT and d) high-magnification HRTEM image showing *b* - *c* plane for TNO15-HT. Dashed lines indicate some intergrowth directions.

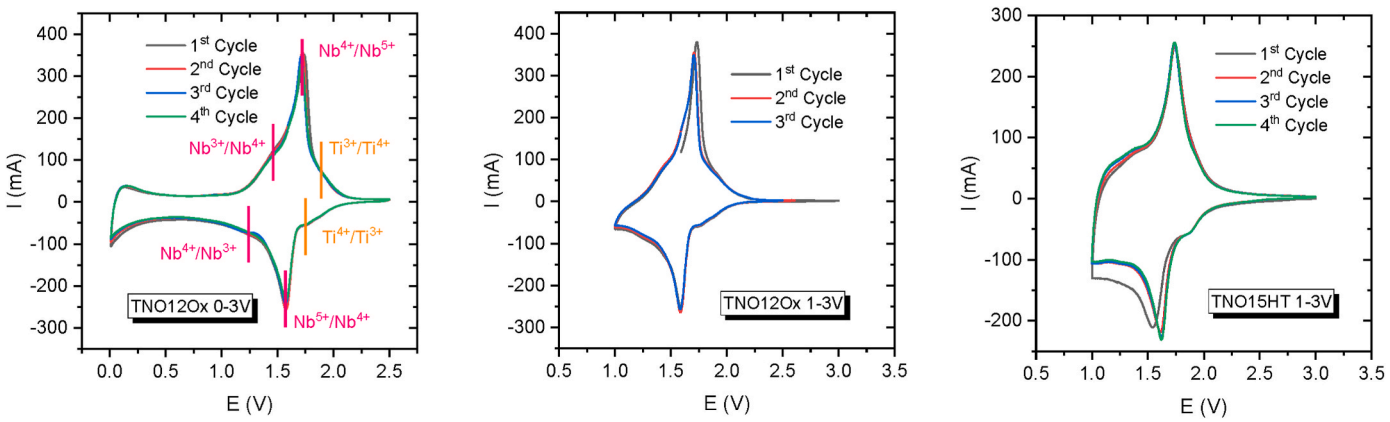

Fig. 6. CV curves for a) TNO12Ox cycled between 0 and 3 V with the characteristic faradaic peaks marked (Nb in purple, Ti in orange); b) TNO12Ox cycled between 1 and 3 V, c) TNO15HT cycled between 1 and 3 V.

the X-ray diffraction (XRD) patterns and Raman spectra for all synthesized titanium–niobium oxide (TNO) materials. To verify the successful synthesis of the target compounds, reference data corresponding to the relevant polymorphs of the binary oxides TiO_2 and Nb_2O_5 have been included in Figs. S1 and S2, respectively, within the Supplementary Information. As shown in Fig. 4(a), the normalized XRD patterns do not correspond to maxima of the individual oxides, but match with the expected maxima for the two TNO compositions targeted. In fact, the diffractograms of the samples obtained via both synthesis routes of $TiNb_2O_7$ match with the reference diffractogram of its monoclinic phase (PDF 01-072-0116). Similarly, $Ti_2Nb_{10}O_{29}$ samples align with the reference diffractogram for the monoclinic phase of this composition (PDF 01-072-0159). However, the XRD reflections of the diffractograms of each route present a clear difference. The solid-state synthesis results in sharply defined peaks, whereas the hydrothermal samples exhibit broader peaks with significantly greater widths. Thus, a larger crystallite size is inferred for both compositions synthesized by the solid-state route compared to the hydrothermal one [19]. This observation is consistent with the SEM images in Fig. 2, where the small crystallites from hydrothermal synthesis correspond to nanoparticle agglomerates, whereas the larger domains in the solid-state samples correspond to microcrystals.

Raman spectra presented in Fig. 4(b) and Fig. S2 also discard the presence of a binary oxides mixture. The representative Raman spectra of all the samples show the features ascribed to the different vibration modes of TNOs [9]. No peaks related to TiO_2 crystalline structures (anatase or rutile) have been detected, indicating a good incorporation of Ti atoms in the Wadsley-Roth structure. Different characteristic zones of the vibrational modes have been identified [20]. Vibrations located in the region below 200 cm^{-1} are associated to the external vibrational modes, while vibrations with frequencies above 200 cm^{-1} are related to the internal modes of the octahedra that construct the Wadsley-Roth structure [9]. This last region can be subdivided into three characteristic subregions: between 200 cm^{-1} and 450 cm^{-1}, ascribed to the bending modes of the octahedron [21]; between 450 cm^{-1} and 900 cm^{-1}, associated to the stretching modes [21]; and modes with frequencies greater than 900 cm^{-1} are related to the vibrational modes of the Nb octahedra at the crystallographic shear planes [22]. Specifically, in TNOs materials, bending modes involve both cations in the structure (Nb, Ti), whereas the stretching modes have more differentiated frequency regions. According to Ref. [9], bands centred at 540 and 650 cm^{-1} are ascribed to Ti corner-shared and edge-shared octahedra, respectively. On the other hand, bands located at 899 and 996 cm^{-1} are related to Nb corner-shared and edge-shared octahedra, respectively. Additionally, stretching modes of Nb octahedra can be found between 600 and 700 cm^{-1} [21], being then the higher frequency modes related to Nb octahedra with higher degree of distortion according to Ref. [21].

As observed in the XRD diffractograms, the Raman spectra of the solid-state synthesized samples appear more defined than those of the hydrothermal samples, particularly in the region below 200 cm^{-1} (external modes). This difference may be related to variations in crystallite size obtained through each synthesis route. When the crystallite is larger, the octahedral structure accommodates more precisely within the monoclinic unit cell, similar to a microcrystal. In contrast, when the crystallite is smaller, the unit cell may be more distorted, leading to a less organized arrangement of octahedra within the crystal structure. However, in both cases, the octahedral units remain present, so their internal vibrations appear regardless of crystallite size. It is worth noting that the Wadsley-Roth structure is inherently described as an arrangement of distorted octahedra [21,23], which explains the broad bands observed in the bending and stretching regions for the two synthesis routes.

To complement the observations from SEM, XRD and Raman measurements, HRTEM images have been collected (Fig. 5(a)–(d), $Ti_2Nb_{10}O_{29}$ samples). HRTEM images of particles for each synthesis method show a clear difference in size, confirming the synthesis of microcrystals by the solid-state route and the synthesis of nanoparticle agglomerates by the hydrothermal route (see Fig. S3 (a)–(c)). This difference is also evident when comparing the electron diffraction patterns of insets in Fig. 5(b) and (c). The diffraction pattern of the solid-state samples displays well defined dots, whereas the one for hydrothermal samples presents concentric rings related to a polycrystalline arrangement. Additionally, a well-organized crystal structure can be identified in the HRTEM images of the solid-state samples (Fig. 5(a)–(b)). By aligning the sample along two different zone axis (*c*-axis in Fig. 5(a) and b-axis in Fig. 5(b)) interplanar distances can be measured and related to the lattice parameter of $Ti_2Nb_{10}O_{29}$ phase ($a = 1.557$ nm, $b = 0.381$ nm, $c = 2.054$ nm, $\beta = 113.68°$). Indeed, in the orientation along c-axis and assuming each white spot in the image represents an octahedron, the 4 × 3 ReO_3-type blocks characteristic of $Ti_2Nb_{10}O_{29}$ structure can be indicated (yellow rectangles in Fig. 5(b)).

For hydrothermal samples (Fig. 5(c)–(d)), orienting the sample is more challenging due to its nanocrystalline nature and the higher number of planar defects observed (Fig. 5(d)). Despite this, interplanar distances in agreement with *b* and *c* axes can be identified. Planar defects in titanium niobium oxides have already been reported and attributed to the random intergrowth of closely related phases [11]. Previous studies [24] have related this highly defective structure to enhanced high-rate capability in LIBs of TNOs.

3.2. Electrochemical characterization

3.2.1. Cycling performance

To study the oxidation-reduction process of the TNO in the lithium

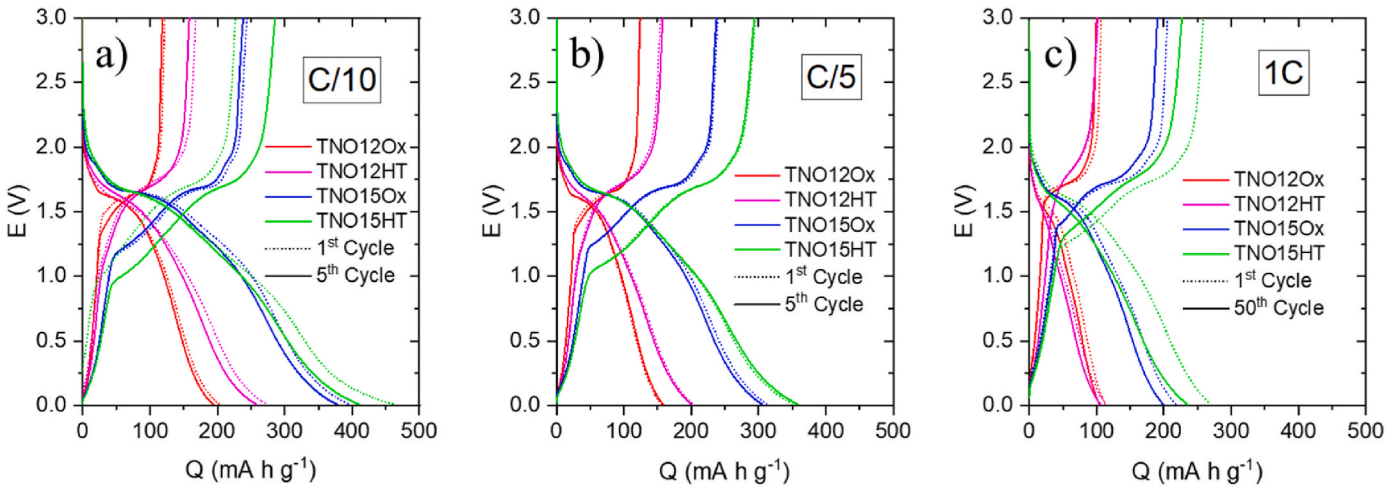

Fig. 7. 1st and 5th GCPL curves for each composition at a) C/10, b) C/5 cycling densities; c) 1st and 50th GCPL curves for each composition at 1C cycling density.

Table 3
GCPLs discharge capacity values for each initial and last cycles at different cycling densities and voltages between 0 and 3V. The charge-discharge performance is displayed in Fig. S5–S8.

	C/10	C/5	1C
	Q mA h g^{-1} *(Number of Cycle)*		
TNO12Ox	203.3 *(1st)*	155.5 *(1st)*	112.9 *(1st)*
	193.7 *(5th)*	158.0 *(5th)*	104.1 *(50th)*
TNO12HT	273.3 *(1st)*	204.1 *(1st)*	113.3 *(1st)*
	258.1 *(5th)*	200.8 *(5th)*	105.4 *(50th)*
TNO15Ox	394.9 *(1st)*	313.4 *(1st)*	217.4 *(1st)*
	377.5 *(5th)*	305.1 *(5th)*	199.1 *(50th)*
TNO15HT	461.0 *(1st)*	351.4 *(1st)*	270.2 *(1st)*
	410.3 *(5th)*	358.0 *(5th)*	234.6 *(50th)*

half-cell cyclic voltammetry (CV) has been employed. As shown in Fig. 6 and Fig. S4, at a sweeping rate of 0.1 mV s^{-1} all the characteristic redox peaks of the titanium are clearly visible regardless of composition and synthesis route. While the oxidation Nb^{4+}/Nb^{5+} and reduction Nb^{5+}/Nb^{4+} are the only transitions shown as peaks, the rest can be clearly seen as shoulders. Prominent peaks indicate fast, well-defined redox reactions, while shoulder features suggest slower or less efficient processes. Moreover, these peaks and shoulders are more defined in the solid-state reaction obtained samples as it can be seen in Fig. 6(a), (b) and (d), which is attributed to the larger crystallite size of the microcrystals compared to the nanoparticle agglomerates obtained via the hydrothermal method (Fig. 6(c) and (e)). Faradaic peaks provide information on the oxidation-reduction voltage of each element in the studied electrodes. As it is marked in Fig. 6(a), the niobium oxidation-reduction voltages are: 1.7 V for Nb^{4+}/Nb^{5+} (oxidation, anodic process, Li^+ disinsertion), 1.6 V for Nb^{5+}/Nb^{4+} (reduction, cathodic process, Li^+ insertion), 1.5 V for Nb^{3+}/Nb^{4+} (oxidation, anodic process, Li^+ disinsertion) and 1.3 V for Nb^{4+}/Nb^{3+} (reduction, cathodic process, Li^+ insertion). Also, the titanium faradaic peaks are located at 1.9 V for Ti^{3+}/Ti^{4+} (oxidation, anodic process, Li^+ disinsertion) and 1.8 V for Ti^{4+}/Ti^{3+} (reduction, cathodic process, Li^+ insertion). All observed peaks correspond to the characteristic lithiation and delithiation regions of the material [25,26].

When the CV experiment is conducted at cut-off voltages below 1 V (Fig. 6(a)), a pseudocapacitive region emerges giving rise to a possible increase in capacity. Indeed, expanding the potential range down to 0.01 V has been identified as a potential strategy for ensuring efficient lithium insertion into the electrode material and to partially avoid the solid-electrolyte interphase (SEI) formation [25,26]. In this sense, it is challenging to obtain a good performance without the need of extending the voltage out of the 3–1 V interval. Thus, we have first evaluated the cycling response of the anode materials in the expanded potential range. The complementary assessment of the behaviour in the 1–3 V range for selected samples is further carried out.

Therefore, to understand the capacity response of each sample, GCPLs have been studied at multiple current rates. As mentioned above, GCPL curves have been studied in the voltage range of 0–3 V (to maximize Li^+ insertion) at three different cycling speeds. As shown in Fig. 7, all the samples have undergone the same cycling protocol, which consists of 5 cycles at C/10 cycling rate followed by another 5 cycles at C/5 and finally, 50 cycles at a 1C rate.

The GCPL data of Fig. 7 show a similar cycling response, with capacity values varying depending on the TNO composition and synthesis route. As shown in Table 3, a significant difference in the capacity of each composition is observed, which can be explained by the theoretical capacity values of $TiNb_2O_7$ and $Ti_2Nb_{10}O_{29}$ which are 387 and 396 mA h g^{-1}, respectively [5]. This corresponds to the insertion of 5 (for $TiNb_2O_7$) and 22 (for $Ti_2Nb_{10}O_{29}$) lithium ions per chemical formula. The capacity also depends on the sample morphology. Microcrystals exhibit lower capacity than nanoparticle agglomerates at all cycling rates. This effect can be explained by the optimization of the oxidation-reduction reaction when the surface to volume ratio of the material is maximized (like in this case, the nanoparticle agglomerates have more surface area than the microcrystals) until particle volume becomes too small to accommodate significant Li^+ insertion. Conversely, the engineering of planar defects has been previously identified as an effective strategy for enhancing capacity [22], primarily by mitigating volume expansion effects. In the present study, the samples synthesized via hydrothermal methods exhibit a higher concentration of planar defects, as evidenced by HRTEM (Fig. 5), which consequently correlates with an improved electrochemical performance.

The capacity observed for the first cycles in the sample TNO15HT exceeds the theoretical value of $Ti_2Nb_{10}O_{29}$ (396 mA h g^{-1}): ranging from 461 to 410.3 mA h g^{-1} at a C/10 current density. This phenomenon can be explained by a SEI formation while cycling in slow current densities [25]. SEI formation has been observed when cycling under 1 V in previous studies [8]. It occurs due electrolyte decomposition, leading to the formation at the electrode surface of different phases which can accommodate Li ions, temporally increasing capacity values while this reaction persists.

A more detailed GCPL study has been performed for all samples, presented in Fig. S5–S8. From this study, the TNO15HT sample shows the best capacity values (>200 mA h g^{-1}) after 200 and 300 cycles with low losses in capacity (≈23 %). This confirms TNO15HT sample as the best performing in this study.

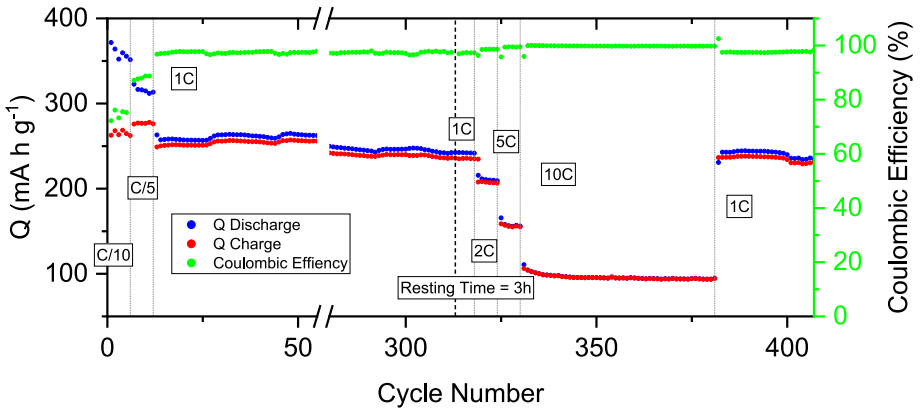

Fig. 8. TNO15HT long cycling study of capacity and coulombic efficiency measurements when cycling between 1 V and 3 V.

Table 4
Comparison of the performance of different TNO materials.

Material	Preparation	Cycling performance	Rate performance	Potential range (V)	Ref
$TiNb_2O_7$	Mineral extraction + Anneling	104 mA h g^{-1} 1C 300 cycles	203 mA h g^{-1} 1C	1–3	[27]
$Ti_2Nb_{10}O_{29}$	Mineral extraction + Anneling	100 mA h g^{-1} 1C 300 cycles	216 mA h g^{-1} 1C	1–3	[27]
$TiNb_2O_7$	Solid-State	195.5 mA h g^{-1} 1C 500 cycles	124 mA h g^{-1} 20C	1–3	[28]
$TiNb_2O_7$@AC	Hydrothermal + Calcination	290 mA h g^{-1} 0.5C 500 cycles	186 mA h g^{-1} 6C	1–3	[29]
$Ti_2Nb_{10}O_{29}$@AC	Hydrothermal	315 mA h g^{-1} 1C 1000 cycles	205 mA h g^{-1} 40C	1–2.5	[30]
$TiNb_2O_7$	Hydrothermal	75 mA h g^{-1} 1C 300 cycles	–	0.01–3	This study
$Ti_2Nb_{10}O_{29}$	Hydrothermal	242.3 mA h g^{-1} 1C 300 cycles	96.1 mA h g^{-1} 10C	1–3	This study

Given the good performance and recovery observed in Fig. S8, TNO15HT sample has been cycled between 1 V and 3 V in a long-term study at higher current rates. This study, shown in Fig. 8, follows the cycling protocol: 5 times at C/10, 5 times at C/5, 300 times at 1C, then rested for 3 h and cycled again 5 times at 1C, 5 times at 2C, 5 times at 5C, 50 times at 10C and 25 times at 1C. The experimental protocol was selected based on our previous experience with similar systems. A 3 h pause was incorporated during the 1C cycling to evaluate whether the capacity could recover during a resting period, which, in this case, was indeed observed. For the same purpose, an additional 1C cycling test was performed following the 10C cycling, and the results confirmed a complete recovery of the capacity at the 1C rate.

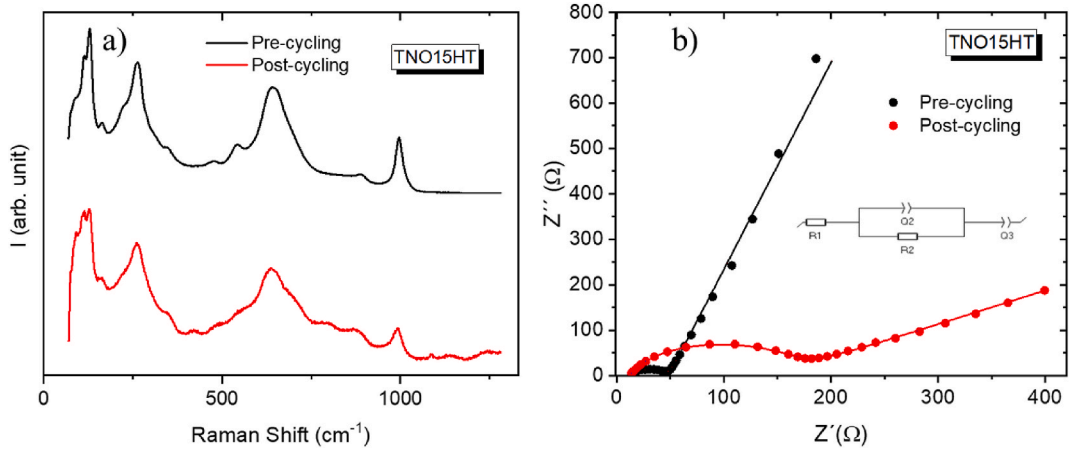

Fig. 9. a) μ-Raman spectra of TNO15HT electrode before and after cycling. b) Nyquist plots of TNO15HT electrodes before and after cycling.

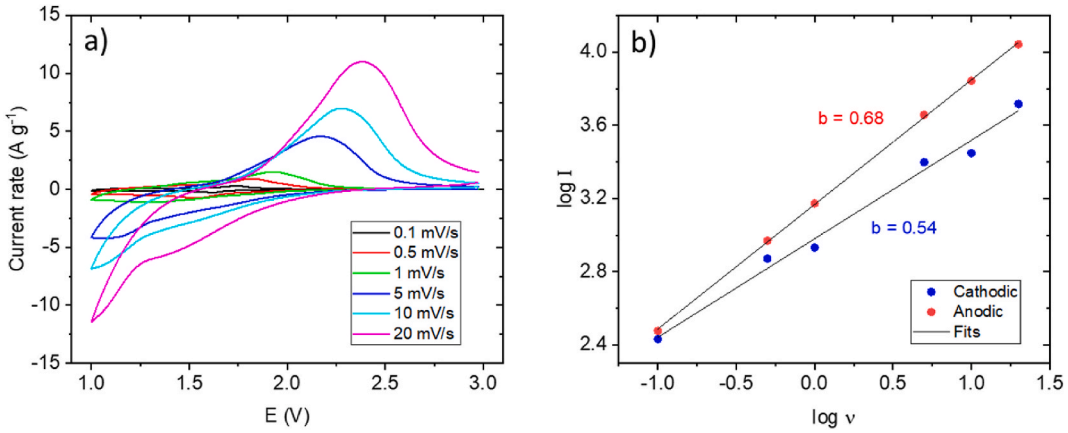

Fig. 10. a) Profiles at rates ranging from 0.1 to 20 mV s^{-1}. b) log(*I*) versus log(*υ*) curves and corresponding fittings for the most prominent anodic and cathodic peaks, indicating the result for *b* parameter from linear fitting.

As seen in Fig. 8, discharge capacity losses remain below 4 % after 200 cycles at 1C and below 6 % after 300 cycles at 1C, while maintaining a coulombic efficiency of 99 %. These results are significantly better than those obtained when cycling between 0.01 V and 3 V. At the highest cycling rate (10C), performance is significantly better between 1 V and 3 V, with capacity values around 100 mA h g^{-1}, compared to less than 50 mA h g^{-1} when cycling between 0.01 V and 3 V. This fact could be rationalized by considering that, at high rates, there is insufficient time for over-lithiation. Thus, while increasing the voltage range does not yield any significant benefits, it does require maintaining each measurement for a longer duration and, particularly at long-term cycling, this may ultimately accelerate degradation. Complete capacity recovery is observed when the cycling rate returned from 10C to 1C after 50 cycles (from 241.6 mA h g^{-1} before 10C to 242.9 mA h g^{-1} after 10C).

A comparison of the results obtained in this work with those found in the literature (with similar morphology and synthesis routes) is presented in Table 4.

3.2.2. *Post-cycling assessment*

To analyse the structural changes in the TNO15HT electrode material after long-term cycling, Raman and EIS measurements have been conducted before and after CV experiments (sequence of CV experiments: 0.1, 0.2, 1, 2, 5, 10, 20, 50 and 100 mV s^{-1}). In Fig. 9(a), Raman spectra of TNO15HT sample shows the same characteristic regions of the TNO structure, as described before. Some subtle differences are appreciated, mainly less defined bands in the post-cycling material. This can be attributed to local lattice deformation caused by repeated lithium-ion insertion. In fact, there are some differences between pre- and post-cycling spectra that point towards the deformation of the metal-oxide polyhedra. First, the broad shoulder appearing between 750 and 800 cm^{-1} is related to vibrations of highly distorted polyhedra with different oxidation numbers ([NbO_6], [NbO_7], and [NbO_8]), typical of low crystalline phases [31]. This is consistent with the increased width observed for all the bands. Additionally, an increase in intensity around 400-500 cm^{-1} appears in the Raman spectra of low-crystalline, distorted octahedra niobium oxides [31]. Nevertheless, the post-cycling spectrum remains similar to the pre-cycling one, indicating good structural stability of the electrode.

In Fig. 9(b) Nyquist plots of TNO15HT composite electrodes before and after cycling (sequence of CV experiments: 0.1, 0.2, 1, 2, 5, 10, 20, 50 and 100 mV s^{-1}) are presented. As can be observed, the Nyquist plots are composed of a depressed semicircle in the medium-high frequency range and a straight sloping line in the low frequency range. The data could be fitted considering the equivalent circuit presented in the inset of Fig. 9(b). The high frequency resistance (R1 in the scheme) is related to the contribution from the electrolyte and electrode, the medium frequency resistance (R2) corresponds to the charge transfer resistance at the electrode/electrolyte interface, and the sloped line (Warburg component in the precycled anode) can be assigned to the solid diffusion process of lithium ions in the active material [32]. The charge-transfer values obtained for the pre- and post-cycled electrode are 38 and 139 Ω, respectively. This increase evidence the deterioration process of ionic transport through components and across interfaces and can be associated with the kinetic hindering caused by the enrichment in insulating constituents.

Aiming to further analyse the kinetics of Li^+ ions storage in the TNO15HT electrode, CV measurements have been carried out at different sweep rates (υ). Fig. 10(a) shows the CV profiles at rates ranging from 0.1 to 20 mV s^{-1}.

The difference in height between the oxidation and reduction peaks can be related to kinetic features, as previously described [33]. The overall kinetics of the stored charge can be divided into two distinct mechanisms: the surface-induced capacitance process and the diffusion-controlled insertion process. Generally, the relationship between the cathodic or anodic peak current (*I*) and the sweeping rate (υ) is described by the following equation:

$$I = a\,\upsilon^{b}$$

Where *a* and *b* are adjustable parameters. The *b* parameter can be obtained from the slope of the log(*I*) versus log(*υ*) curve. Based on earlier research [34], a *b* value close to 1 means that the system is mainly controlled by the capacitance process, whereas a *b* value approaching 0.5 points to a dominating diffusion-controlled process. Therefore, intermediate values between 0.5 and 1 suggest a mixed kinetics process. Fig. 10(b) shows the log(*I*) versus log(*υ*) curves and corresponding fittings for the most prominent anodic and cathodic peaks. The obtained *b*-values for the reduction and the oxidation processes are 0.68 and 0.54, respectively, revealing that charge storage partially arises from surface capacitive effects.

3.2.3. *Preliminary temperature measurements*

Operating at low temperatures under high-rate conditions presents a significant limitation for lithium-ion batteries, particularly concerning their use in winter and in cold climates [35]. On the other hand, LIBs showing good performance at temperatures higher than RT are also interesting, especially for use in summer and hot climates. Elevated temperatures typically speed up chemical reactions within the battery, reducing its capacity to retain a charge over repeated cycles. This effect is especially critical for lithium-ion batteries, as excessive heat can lead to capacity loss and a diminished lifespan [36].

In this sense, a battery capable operating in a large temperature range with high performance and good capacity recovery is of great

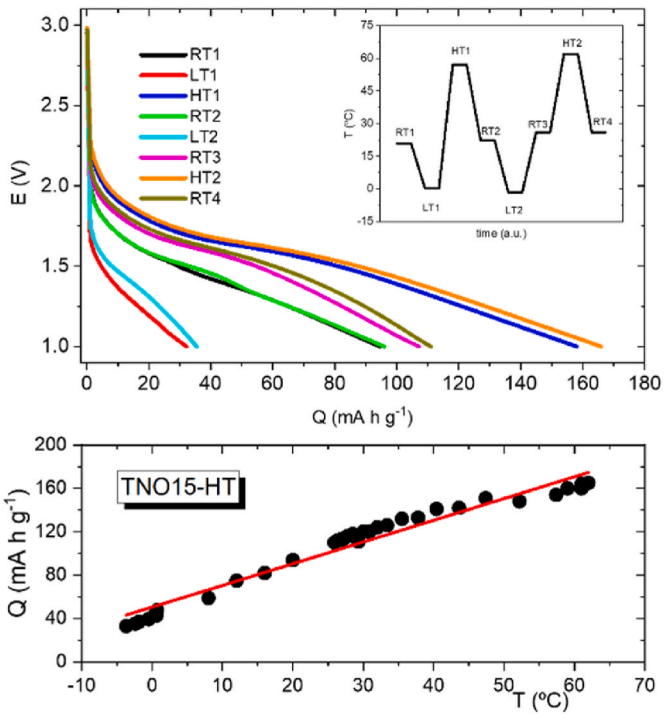

Fig. 11. a) Potential vs discharge capacity profiles at 1C for the TNO15-HT electrode at different temperatures. RT, LT and HT refer to room-, low- and high-temperature, respectively. The inset shows the sequence of heating and cooling with time. b) Variation of the discharge specific capacity with temperature. The line is a guide to the eye for appreciating quasi-linearity.

interest. Encouraged by this, as a preliminary study, we have conducted several experiments to assess the performance of the TNO15-HT electrode at different temperatures, ranging between −5 °C (LT) and 60 °C (HT), as shown in Fig. 11. The discharge curves were recorded after 1 h of temperature stabilization. The battery shows an increase in capacity upon heating, whereas a significant decrease is observed at low temperatures (Fig. 11(a)). The variation of specific capacity with temperature follows a linear trend (Fig. 11(b)). More interestingly, the battery demonstrates the ability to recover its original capacity once it returns to room temperature, even after being cycled at low or high temperatures. Although the device does not provide high capacity at low temperatures, it is not damaged during operation under these conditions. This is a desirable characteristic for batteries, particularly for applications such as electric vehicles.

4. Conclusions

Titanium niobium oxides with the stoichiometries $TiNb_2O_7$ and $Ti_2Nb_{10}O_{29}$ have been successfully obtained via solid-state and hydrothermal synthesis. In the solid-state synthesis, the process was initiated with binary oxides, while in the hydrothermal method, niobium oxalate hydrate and titanium acetylacetonate were used as precursors.

The solid-state route produced microcrystals with some heterogeneity in composition, while hydrothermal synthesis resulted in nanoparticle agglomerates with a homogeneous composition. XRD, Raman and HRTEM measurements confirm the characteristic features of Wadsley-Roth structures for both compositions. Solid-state samples display high crystallinity, whereas hydrothermal samples show a defective structure with high concentration of planar defects.

The comparison of the electrochemical performance of the samples indicates that hydrothermal samples exhibit the highest capacity for lithium insertion. Special attention has been given to hydrothermally synthesized $Ti_2Nb_{10}O_{29}$, which demonstrates the best performance as a lithium-ion battery electrode when cycled between 1 V and 3V. With capacity values around 250 mA h g^{-1} at 1C cycling and a coulombic efficiency of 99 %, it retains >94 % of its capacity after 300 cycles at 1C and shows complete capacity recovery after reverting from 50 cycles at 10C back to 1C cycling. The superior performance of this sample can be attributed to its nanoparticulate morphology, which enhances lithium diffusion into the particles, along with its defective crystal structure, which may further facilitate lithium transport. The material's high stability and recovery have been demonstrated, even under low and high temperatures and during long-term cycling.

CRediT authorship contribution statement

A. Calvo-Villoslada: Writing – review & editing, Writing – original draft, Visualization, Validation, Methodology, Investigation, Formal analysis, Data curation. **M.L. López:** Writing – review & editing, Validation, Resources, Methodology, Investigation, Funding acquisition, Conceptualization. **P. Almodóvar:** Writing – review & editing, Validation, Resources, Methodology. **P. Fernández:** Writing – review & editing, Visualization, Validation, Supervision, Resources, Conceptualization. **I. Álvarez-Serrano:** Writing – review & editing, Writing – original draft, Visualization, Validation, Supervision, Resources, Methodology, Investigation, Formal analysis, Conceptualization. **B. Sotillo:** Writing – review & editing, Writing – original draft, Visualization, Validation, Supervision, Project administration, Methodology, Investigation, Formal analysis, Data curation, Conceptualization.

Declaration of competing interest

The authors declare that they have no known competing financial interests or personal relationships that could have appeared to influence the work reported in this paper.

Acknowledgements

The authors are grateful to Complutense University of Madrid for support via the Project PR3/23–30813 and to the Project CPP2022-009910 financed by MCIN/AEI/10.13039/501100011033 and by NextGeneration EU/PRTR. The authors would like to thank the UCM CAI of X-Ray diffraction for performing the XRD measurements, and the UCM ICTS of Microscopy for carrying out HRTEM.

Appendix A. Supplementary data

Supplementary data to this article can be found online at https://doi.org/10.1016/j.mtchem.2025.102860.

Data availability

The data that support the findings of this study are available from the corresponding author upon reasonable request.

References

[1] N. Nasajpour-Esfahani, H. Garmestani, M. Bagheritabar, D.J. Jasim, D. Toghraie, S. Dadkhah, H. Firoozeh, Comprehensive review of lithium-ion battery materials and development challenges, Renew. Sustain. Energy Rev. 203 (2024) 114783, https://doi.org/10.1016/J.RSER.2024.114783.

[2] K.J. Griffith, Y. Harada, S. Egusa, R.M. Ribas, R.S. Monteiro, R.B. Von Dreele, A. K. Cheetham, R.J. Cava, C.P. Grey, J.B. Goodenough, Titanium niobium oxide: from discovery to application in fast-charging lithium-ion batteries, Chem. Mater. 33 (2021) 4–18, https://doi.org/10.1021/acs.chemmater.0c02955.

[3] X. Zhang, J. Sun, Z. Cheng, M. Wu, Z. Guo, H. Zhang, Design, perspective, and challenge of niobium-based anode materials for high-energy alkali metal-ion batteries, Adv. Funct. Mater. 34 (2024) 2405392.

[4] P.U. Nzereogu, A.D. Omah, F.I. Ezema, E.I. Iwuoha, A.C. Nwanya, Anode materials for lithium-ion batteries: a review, Appl. Surf. Sci. Adv. 9 (2022) 100233, https://doi.org/10.1016/j.apsadv.2022.100233.

[5] C. Peng, S. Liang, Y. Yu, L. Cao, C. Yang, X. Liu, K. Guo, P. Müller-Buschbaum, Y.-J. Cheng, C. Wang, A chronicle of titanium niobium oxide materials for high-performance lithium-ion batteries: from laboratory to industry, Carbon Neutralization 3 (2024) 1036–1091, https://doi.org/10.1002/cnl2.177.
[6] A. Khan, S. Yaqub, M. Ali, A.W. Ahmad, H. Nazir, H.A. Khalid, N. Iqbal, Z. Said, K. Sopian, A state-of-the-art review on heating and cooling of lithium-ion batteries for electric vehicles, J. Energy Storage 76 (2024) 109852, https://doi.org/10.1016/J.EST.2023.109852.
[7] A.D. Wadsley, Mixed oxides of titanium and niobium. I, Acta Crystallogr. 14 (1961) 660–664.
[8] Y. Yang, J. Zhao, Wadsley–roth crystallographic shear structure niobium-based oxides: promising anode materials for high-safety lithium-ion batteries, Adv. Sci. 8 (2021), https://doi.org/10.1002/advs.202004855.
[9] N.G. Eror, U. Balachandran, Coordination of cations in TiNb2O7 by Raman spectroscopy, J. Solid State Chem. 45 (1982) 276–279, https://doi.org/10.1016/0022-4596(82)90283-3.
[10] R.B. Von Dreele, A.K. Cheetham, The structures of some titanium-niobium oxides by powder neutron diffraction, Proceedings of the Royal Society of London. A. Mathematical and Physical Sciences 338 (1974) 311–326.
[11] J.G. Allpress, Mixed oxides of titanium and niobium: intergrowth structures and defects, J. Solid State Chem. 1 (1969) 66–81, https://doi.org/10.1016/0022-4596(69)90010-3.
[12] S.H. Choi, B. Ali, K.S. Choi, S.K. Hyun, J.J. Sim, W.J. Choi, W. Joo, J.H. Lim, T. H. Lee, T.S. Kim, K.T. Park, Reaction kinetics and morphological study of TiNb2O7 synthesized by solid-state reaction, Arch. Metall. Mater. 62 (2017) 1051–1056, https://doi.org/10.1515/amm-2017-0152.
[13] K. Momma, F. Izumi, VESTA 3 for three-dimensional visualization of crystal, volumetric and morphology data, J. Appl. Crystallogr. 44 (2011) 1272–1276, https://doi.org/10.1107/S0021889811038970.
[14] Y. Sheng, Y. Wang, S. Yin, L. Zhao, X. Zhang, D. Liu, G. Wen, Niobium-based oxide for anode materials for lithium-ion batteries, Chem. Eur J. 30 (2023) e202302865, https://doi.org/10.1002/chem.202302865.
[15] H. Ding, Z. Song, H. Zhang, X. Li, Niobium-based oxide anodes toward fast and safe energy storage: a review, Mater Today Nano 11 (2020) 100082, https://doi.org/10.1016/j.mtnano.2020.100082.
[16] A.J. Green, E.H. Driscoll, Y. Lakhdar, E. Kendrick, P.R. Slater, Cite this, Dalton Trans. 52 (2023) 13110, https://doi.org/10.1039/d3dt02144k.
[17] K. Ise, S. Morimoto, Y. Harada, N. Takami, Large lithium storage in highly crystalline TiNb2O7 nanoparticles synthesized by a hydrothermal method as anodes for lithium-ion batteries, Solid State Ionics 320 (2018) 7–15, https://doi.org/10.1016/J.SSI.2018.02.027.
[18] C.Y. Ou, K.K. Gupta, C.H. Lu, Structure, morphology, and electrochemical characterization of anatase TiO2-coated TiNb2O7 for lithium-ion batteries, Ceram. Int. 50 (2024) 23400–23407, https://doi.org/10.1016/J.CERAMINT.2024.04.062.
[19] T.-F. Yi, Y. Xie, J. Shu, Z. Wang, C.-B. Yue, R.-S. Zhu, H.-B. Qiao, Structure and electrochemical performance of niobium-substituted spinel lithium titanium oxide synthesized by solid-state method, J. Electrochem. Soc. 158 (2011) A266, https://doi.org/10.1149/1.3533391.
[20] B. Sotillo, R. Ariza, P. Fernández, J. Solis, Ultrafast-laser powder bed fusion of oxygen-deficient Nb2O5 ceramics with highly improved electrical properties, Mater. Des. 224 (2022) 111346, https://doi.org/10.1016/J.MATDES.2022.111346.
[21] J.M. Jehng, I.E. Wachs, Structural chemistry and Raman spectra of niobium oxides, Chem. Mater. 3 (1991) 100–107, https://doi.org/10.1021/cm00013a025.
[22] S. Andersson, J. Galy, Wadsley defects and crystallographic shear in hexagonally close-packed structures, J. Solid State Chem. 1 (1970) 576–582, https://doi.org/10.1016/0022-4596(70)90144-1.
[23] Y. Yang, J. Zhao, Wadsley–Roth crystallographic shear structure niobium-based oxides: promising anode materials for high-safety lithium-ion batteries, Adv. Sci. 8 (2021) 2004855.
[24] T. Li, G. Nam, K. Liu, J.-H. Wang, B. Zhao, Y. Ding, L. Soule, M. Avdeev, Z. Luo, W. Zhang, T. Yuan, P. Jing, M.G. Kim, Y. Song, M. Liu, A niobium oxide with a shear structure and planar defects for high-power lithium ion batteries, Energy Environ. Sci. 15 (2022) 254–264, https://doi.org/10.1039/D1EE02664J.
[25] H. Aghamohammadi, N. Hassanzadeh, R. Eslami-Farsani, A comprehensive review study on pure titanium niobium oxide as the anode material for Li-ion batteries, J. Alloys Compd. 911 (2022) 165117, https://doi.org/10.1016/j.jallcom.2022.165117.
[26] D. Pham-Cong, J. Kim, V.T. Tran, S.J. Kim, S.Y. Jeong, J.H. Choi, C.R. Cho, Electrochemical behavior of interconnected Ti2Nb10O29 nanoparticles for high-power Li-ion battery anodes, Electrochim. Acta 236 (2017) 451–459, https://doi.org/10.1016/J.ELECTACTA.2017.03.203.
[27] B. Sotillo, J. Calbet, I. Álvarez-Serrano, I. García-Díaz, P. Fernández, F.A. López, Exploring titanium niobium oxides recovered from columbotantalite mineral as lithium-ion batteries electrodes, Ceram. Int. 50 (2024) 32783–32792, https://doi.org/10.1016/J.CERAMINT.2024.06.088.
[28] L.-Q. Cheng, Y. He, K. Chen, Z. Ma, R. Liu, N. Liu, Y. Deng, Facile fabrication of a high performance TiNb2O7 anode for large-scale electrical energy storage, J Mater Chem A Mater 10 (2022) 17586–17592, https://doi.org/10.1039/D2TA03995H.
[29] J. Luo, J. Peng, P. Zeng, Z. Wu, J.Y. Li, W. Li, Y. Huang, B. Chang, X. Wang, TiNb2O7 nano-particle decorated carbon cloth as flexible self-support anode material in lithium-ion batteries, Electrochim. Acta 332 (2020) 135469, https://doi.org/10.1016/J.ELECTACTA.2019.135469.
[30] S. Shi, G. Wang, G. Wan, Y. Tang, G. Zhao, Z. Deng, J. Chai, C. Wei, G. Wang, Titanium niobate (Ti2Nb10O29) anchored on nitrogen-doped carbon foams as flexible and self-supported anode for high-performance lithium ion batteries, J. Colloid Interface Sci. 587 (2021) 622–632, https://doi.org/10.1016/J.JCIS.2020.11.019.
[31] J.M. Jehng, I.E. Wachs, Structural chemistry and Raman spectra of niobium oxides, Chem. Mater. 3 (1991) 100–107, https://doi.org/10.1021/CM00013A025/ASSET/CM00013A025.FP.PNG_V03.
[32] L.A. Middlemiss, A.J.R. Rennie, R. Sayers, A.R. West, Characterisation of batteries by electrochemical impedance spectroscopy, Energy Rep. 6 (2020) 232–241, https://doi.org/10.1016/J.EGYR.2020.03.029.
[33] W. Tian, J. Tang, B.-N. Park, Citation, B.-N. Park, Unraveling Asymmetric Electrochemical Kinetics in Low-Mass-Loading Unraveling Asymmetric Electrochemical Kinetics in Low-Mass-Loading LiNi 1/3 Mn 1/3 Co 1/3 O 2 (NMC111) Li-Metal All-Solid-State Batteries, 2024, https://doi.org/10.3390/ma17205014.
[34] D.A. Giraldo, P. Almodóvar, I. Álvarez-Serrano, J. Chacón, M.L. López, Electrochemical performance of tunnelled and layered MnO 2 electrodes in aluminium-ion batteries: a matter of dimensionality, J. Electrochem. Soc. 169 (2022) 100538, https://doi.org/10.1149/1945-7111/ac9a7a.
[35] E.A. Pogue, S.A. Langevin, T. Hamann, K.K. Rao, M.A. Schroeder, N.Q. Le, C. McHale, Z. Burchfield, J.S. Ko, Enhancing low-temperature lithium-ion battery performance under high-rate conditions with niobium oxides, Mater. Today Energy 45 (2024) 101663, https://doi.org/10.1016/J.MTENER.2024.101663.
[36] D. Ouyang, J. Weng, M. Chen, J. Wang, Impact of high-temperature environment on the optimal cycle rate of lithium-ion battery, J. Energy Storage 28 (2020) 101242, https://doi.org/10.1016/J.EST.2020.101242.